Volume 7 | Number 22 | 14 June 2019 | Pages 6479–6806

Journal of Materials Chemistry C

Materials for optical, magnetic and electronic devices

rsc.li/materials-c

ISSN 2050-7526

ROYAL SOCIETY OF CHEMISTRY | Celebrating IYPT 2019

PAPER

Donald A. MacLaren, Jan-Willem G. Bos *et al.*

Low thermal conductivity and promising thermoelectric performance in A_xCoSb (A = V, Nb or Ta) half-Heuslers with inherent vacancies

Journal of Materials Chemistry C

PAPER

View Article Online
View Journal | View Issue

Cite this: J. Mater. Chem. C, 2019, 7, 6539

Low thermal conductivity and promising thermoelectric performance in A_xCoSb (A = V, Nb or Ta) half-Heuslers with inherent vacancies†

Daniella A. Ferluccio,[a] John E. Halpin,[b] Kathryn L. MacIntosh,[a] Robert J. Quinn,[a] Eric Don,[c] Ronald I. Smith,[d] Donald A. MacLaren *[b] and Jan-Willem G. Bos *[a]

Received 8th February 2019,
Accepted 8th March 2019

DOI: 10.1039/c9tc00743a

rsc.li/materials-c

Half-Heuslers with vacancies that are stabilised by a semiconducting electron count offer new opportunities for discovering good thermoelectric performance. Here, we present a comparative study of A_xCoSb half-Heuslers (A = V, Nb or Ta) with intrinsic vacancies. Structural analysis reveals an increasing vacancy concentration from V (13%) to Nb (15%) to Ta (19%) with evidence for ~3% V/Co inversion. This decrease in ability to n-type dope these materials is caused by an increase in conduction band dispersion, evident from a decreasing density of states mass from Hall data, leading to a higher cost of populating these antibonding states. $V_{0.87}CoSb$ has an ultralow lattice thermal conductivity, $\kappa_{lat} \sim 2.2$ W m^{-1} K^{-1}, which cannot be explained within the Callaway framework. Coupled to a promising power factor, $S^2/\rho = 2.25$ mW m^{-1} K^{-2}, this results in $ZT = 0.6$ at 950 K. $Nb_{0.85}CoSb$ has a power factor of $S^2/\rho = 2.75$ mW m^{-1} K^{-2} with $\kappa \sim 4.75$ W m^{-1} K^{-1}, yielding a similar $ZT = 0.5$ at 950 K. $Ta_{0.81}CoSb$ has a microstructure consisting of smaller grains than the other samples, impacting both the carrier and thermal transport, yielding a power factor $S^2/\rho = 0.75$ mW m^{-1} K^{-2} and $ZT = 0.3$ at 950 K. The ultralow κ_{lat} for $V_{0.87}CoSb$ may be linked to porosity effects that do not strongly impact on the charge transport, thus affording a new route towards improved performance.

Introduction

Thermoelectric waste heat recovery is one of a range of renewable energy strategies that are currently being developed to reduce reliance on fossil fuels and to mitigate climate change.[1,2] Half-Heuslers (HHs) are leading candidates for commercialisation due to their unique combination of good thermoelectric performance, abundance of constituent elements, good mechanical properties and thermal stability.[3–5] HHs are ternary XYZ compounds typically comprising two transition metals (X and Y) and a main group element (Z) that crystallise in the cubic space group $F\bar{4}3m$ with the electropositive X metals occupying octahedral sites and the Y metals occupying half the tetrahedral sites in a face centred cubic Z lattice.[6] Recently, HH compositions with a nominal 19 valence electron count (VEC), including VCoSb and NbCoSb,[7,8] have attracted attention due to their apparent violation of the long-established 18-electron requirement for semiconducting properties.[6] This was resolved through studies of NbCoSb that demonstrated the formation of Nb vacancies, leading to Nb_xCoSb ($x \sim 0.85$) compositions with VEC ~ 18.25.[9–11] Varying the nominal Nb content between $x = 0.8$ (VEC = 18) and $x = 1$ (VEC = 19) affords a systematic change in carrier concentration (n_H) and a means of optimising the thermoelectric power factor, S^2/ρ, where S is the Seebeck coefficient and ρ is the electrical resistivity.[11] The optimised power factor of $S^2/\rho = 2.4$ mW m^{-1} K^{-2} and low thermal conductivity (κ) resulted in a highly promising thermoelectric figure of merit, $ZT = (S^2/\rho\kappa)T = 0.9$ at 1123 K, demonstrating that vacancies are a new, useful route to tune the individual thermoelectric parameters and achieve good performance. Here, κ is the sum of κ_{lat} and an electronic component (κ_{el}) and T is the absolute temperature. Up to this point optimisation of HHs has been achieved chiefly *via* doping and alloying,[12–14]

[a] Institute of Chemical Sciences and Centre for Advanced Energy Storage and Recovery, School of Engineering and Physical Sciences, Heriot-Watt University, Edinburgh, EH14 4AS, UK. E-mail: j.w.g.bos@hw.ac.uk
[b] SUPA, School of Physics and Astronomy, University of Glasgow, Glasgow G12 8QQ, UK. E-mail: dmaclaren@physics.org
[c] SemiMetrics Ltd, Kings Langley WD4 9WB, UK
[d] ISIS Neutron and Muon Source, Harwell Campus, Didcot OX11 0QX, UK

† Electronic supplementary information (ESI) available: Structural parameters and fit statistics from Rietveld analysis of polaris neutron powder diffraction data; XRD data for the preliminary series of samples, Rietveld fits to polaris NPD data for the A_xCoSb (A = Nb, Ta) samples; complementary larger area SEM images and EDX elemental maps; temperature dependence of the thermal diffusivity, heat capacity, Lorenz number and electronic thermal conductivity. See DOI: 10.1039/c9tc00743a

use of interstitial metals[15] or nanostructuring.[16–19] The vacancy approach is therefore a new route in the portfolio that is not well explored.

We have investigated the concentration of X-site vacancies and thermoelectric properties of the A_xCoSb (A = V, Nb and Ta) compositions allowing for the impact of the A metal to be assessed. A recent study has investigated the structural stability of a range of vacancy HHs.[20] This revealed an increasing cost for filling the X-site from V to Nb to Ta. We confirm the existence of preferred x compositions for the V and Nb compositions and show that A = Ta fits with the proposed trend.[20] The thermoelectric properties of stoichiometric VCoSb have been reported (ref. 8) but the properties of the A_xCoSb (A = V, Ta) compositions with targeted vacancies remain unexplored.

Experimental

Synthesis

A preliminary series of polycrystalline $A_{0.84}CoSb$ (A = V, Nb and Ta) samples was prepared on a 1 gram scale from powdered elements purchased from Alfa Aesar; V: 325-mesh, 99.5% purity; Nb: 325-mesh, 99.8%; Ta: 325-mesh, 99.9%; Co: 1.6 μm, 99.8% and Sb: 1–5 mm shots, 99.99%. This was followed by a 5 gram scale-up of the optimised compositions (see below) to produce $V_{0.87}CoSb$, $Nb_{0.85}CoSb$ and $Ta_{0.81}CoSb$. The initial choice for the $A_{0.84}CoSb$ compositions was based on a survey of the literature for A = Nb, where $0.83 \leq x \leq 0.85$ based on diffraction results.[9,10] In all reactions, stoichiometric amounts of elemental precursors were mixed using an agate pestle and mortar and cold-pressed into 13 mm diameter pellets using a 10 tonne press. Samples were wrapped in Nb (V, Nb samples) or Ta (Ta samples) foil and sintered in vacuum sealed quartz tubes for 24 hours at 1073 K, then cooled at 20 K min^{-1}. The samples were then re-ground, re-sealed and subjected to a further 7 days of sintering at 1123 K before being air-quenched. As a final step, the samples were powdered using mortar and pestle then hot-pressed into two 13 mm disks under an argon atmosphere at 1273 K (Nb and Ta samples) or 1123 K (V sample) and 80 MPa for 30 minutes.

Characterisation

Laboratory X-ray powder diffraction (XRD) data was collected using a D8 Bruker Advance diffractometer with monochromated Cu $K\alpha_1$ radiation. High-quality datasets suitable for Rietveld analysis were collected in the $5^\circ \leq 2\theta \leq 100^\circ$ range over seven hours. Time-of-flight neutron powder diffraction (NPD) patterns were collected on the POLARIS instrument at the ISIS neutron and muon source, Rutherford Appleton Laboratory, UK. Data were collected at room temperature for between 200 and 300 μA proton beam current to the ISIS target, with 1–2 g of powdered sample loaded into cylindrical vanadium cans. This corresponds to an exposure of approximately 1.5–2 hours for each sample. Note that a different A = Nb sample was used for the NPD and Hall study, with nominal $Nb_{0.83}CoSb$ composition. This was due to the timings of these experiments, which were not done in-house. All other data in this manuscript were collected on the A_xCoSb samples with optimised compositions. Rietveld analysis of both XRD and NPD datasets were done using the GSAS and EXPGUI software programs.[21,22]

Microscopy

Scanning electron microscopy (SEM) employing both secondary electron (SE) and backscattered electron (BSE) imaging was performed on samples that were first cut from a hot-pressed disk with a low speed diamond saw to expose an internal face, then mechanically polished (SiC paper followed by alumina, colloidal silica and diamond paste to achieve a flat surface finish). A Thermo Fischer Helios Dualbeam instrument equipped with a Bruker XFlash 100 mm^2 detector was used for energy dispersive X-ray spectroscopy (EDS) analysis of composition and a Bruker eFlash FS Electron back-scattered diffraction (EBSD) detector was used for assessment of crystallography and granularity. EDS analysis was performed using Bruker's Esprit 2.1 software package and a standard-less quantification method to derive compositions that are accurate to 2–3 atomic percent. EBSD images were processed using ATOM,[23] whereby EBSD patterns were fitted to HH structures and pixels were false-coloured to indicate the crystallographic orientation, producing vivid mosaic-like images that clearly discriminate grains and which were then used to assess grain size distributions.

Thermoelectric property measurements

The Seebeck coefficient (S) and electrical resistivity (ρ) were measured on rectangular bars cut from the hot-pressed disks using a Linseis LSR 3 instrument between 320–970 K. Thermal diffusivities (α) were measured on whole hot-pressed disks (~2 mm thickness) using a Linseis LFA 1000 Laser Flash

Table 1 Half-Heusler lattice parameters (a) from X-ray powder diffraction, gravimetric densities (d), percentage densities (d%), chemical compositions from EDX elemental mapping and from Rietveld analysis of X-ray and neutron powder diffraction data for the A_xCoSb (A = V, Nb, Ta) samples investigated in this study

Sample	x	a (Å)	d (g cm^{-3})	d%	EDX composition	Rietveld composition
V_xCoSb	0.84	5.8039(1)				$V_{0.87(1)}CoSb$
	0.87	5.8058(1)	7.2	95	0.87(1):0.99(1):1.00	$[V_{0.838(2)}Co_{0.032(2)}][Co_{0.968(2)}V_{0.032(2)}]Sb$[a]
Nb_xCoSb	0.84	5.9024(1)				$Nb_{0.85(1)}CoSb$
	0.85	5.9023(1)	8.4	100	0.86(1):0.99(1):1.00	$Nb_{0.85(1)}CoSb$
Ta_xCoSb	0.84	5.8888(1)				$Ta_{0.81(1)}CoSb$
	0.81	5.8910(1)	10.7	100	0.89(2):1.02(1):1.00	$Ta_{0.83(1)}CoSb$[a]

[a] Compositions from Rietveld analysis of neutron powder diffraction data.

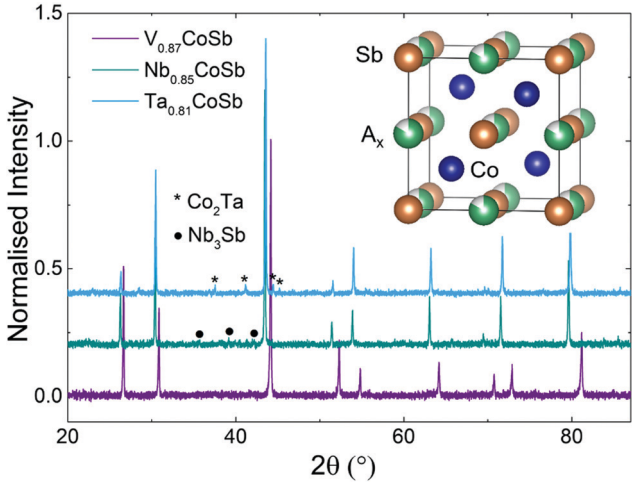

Fig. 1 Laboratory X-ray powder diffraction patterns for $V_{0.87}CoSb$, $Nb_{0.85}CoSb$ and $Ta_{0.81}CoSb$, showing the presence of a major half-Heusler (HH) phase and small Nb_3Sb and Co_2Ta impurity phases. The inset shows a schematic of a HH structure with X-site vacancies.

instrument. The samples were coated with graphite spray to avoid emissivity errors. The densities (d) of the samples were calculated from the dimensions and mass of the pellets and are given in Table 1. The thermal conductivity $\kappa = \alpha C_p d$ was calculated using experimental α and d values, with heat capacity (C_p) values taken from the literature.[8,24] A porosity correction, $\kappa_m/\kappa = (1 - \varphi)/(1 + \varphi/2)$, where κ_m is the uncorrected measured value and ϕ is the porosity taken from the percentage density, was applied for the V sample. Hall measurements were undertaken on 5 × 5 mm^2 square slices in applied fields of ±1 T using an AC Field Hall system from SemiMetrics, Ltd. Silver paint was used to achieve good electrical contacts on the corners of the samples.

Results

XRD

A preliminary series of $A_{0.84}CoSb$ (A = V, Nb, Ta) samples was prepared to check for phase purity and analysis of the crystallographic site occupancies of the HH phase through Rietveld fitting. The XRD patterns for these samples are shown in Fig. S1 in the ESI.† Rietveld analysis of the X-site occupancy suggested a systematic decrease from 0.87(1) for A = V to 0.85(1) for A = Nb and 0.81(1) for A = Ta. In response to these initial results, synthesis of $V_{0.87}CoSb$, $Nb_{0.85}CoSb$ and $Ta_{0.81}CoSb$ was undertaken on a 5 gram scale so that full structural and thermoelectric characterisation could be undertaken. Rietveld analysis of XRD data collected from these samples (the patterns are shown in Fig. 1) confirmed the targeted X-site occupancies. The V and Nb samples have good purity from XRD with only a small Nb_3Sb phase (<1 wt%) observed. The lattice parameter for the $Nb_{0.85}CoSb$ sample (a = 5.902 Å) is in good agreement with the near-constant values reported for Nb_xCoSb (a = 5.903 Å; $0 \leq x \leq 0.2$).[11] The Ta sample contains a 5.3(1) wt% Co_2Ta intermetallic impurity.

NPD

Neutron diffraction is highly complementary to XRD as it offers good scattering contrast between first row transition metals, which is important as V/Co inversion has been suggested to occur.[8] The full results of the Rietveld fits are summarised in Table S1 (ESI†) with the experimental HH compositions given in Table 1. The final fits are shown in Fig. 2 (V sample) and Fig. S2 in the ESI† (Nb and Ta samples). The main result is that the $V_{0.87}CoSb$ sample does indeed have a degree of V/Co inversion with an experimental composition of $[V_{0.838(2)}Co_{0.032(2)}][Co_{0.968(2)}V_{0.032(2)}]Sb$. Free refinement of the X-site occupancy yielded an unrealistic composition of $V_{0.58(1)}CoSb$, which corresponds to a 17-electron HH. HHs with this valence electron count are predicted to be metallic,[6,25] which is not in keeping with the observed semiconducting behaviour. We note that this result is robust against variations in atomic displacement parameter (ADP). For example, fixing the X-site site occupancy at 0.87 leads to ADP values for that

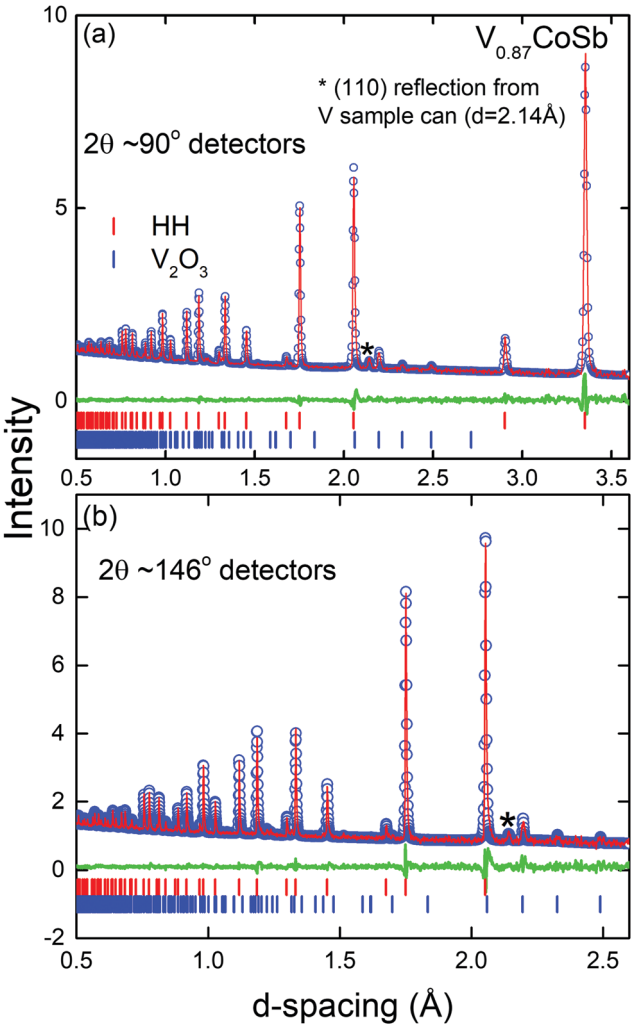

Fig. 2 Fitted Polaris neutron powder diffraction profiles for $V_{0.87}CoSb$ (a) $2\theta \sim 90°$ detectors and (b) $2\theta \sim 146°$ detectors. Blue circles are observed data, red lines are the calculated profile, green lines are the difference profiles (obs-calc). Vertical lines indicate Bragg reflection positions.

site that are unphysically large with respect to those of the other sites. The best way to reconcile the XRD and NPD fits is to assume that the overall $V_{0.87}CoSb$ composition from XRD is maintained and allow for V/Co inversion over the X and Y sites. This yields near identical goodness of fit statistics (see Table S1, ESI†) and indicates the presence of ~3% V/Co inversion. Analysis of the site occupancies for the Nb and Ta samples confirms the XRD results with refined compositions of $Nb_{0.85(1)}CoSb$ and $Ta_{0.83(1)}CoSb$ that are within 1–2 estimated standard deviations of the starting values. The indexed impurity phases include a small V_2O_3 phase (1.1(1) wt%) that had not been noted by XRD and the Nb_3Sb and Co_2Ta phases that were already observed in XRD. The final fits for all samples were compared against a model-less LeBail fit and found to be close to the best possible value for all compositions (Table S1, ESI†).

Scanning electron microscopy

SEM imaging, EBSD and EDX mapping were used to investigate the microstructure and compositions of all three A_xCoSb compositions. Large area ($>200 \times 200\ \mu m^2$) SEM images are shown in Fig. S3 (ESI†); higher magnification images and EBSD data are presented in Fig. 3 with the EDX maps for these areas given in Fig. S4 (ESI†). Several striking trends are discernible in the SEM and EBSD data. First, the $V_{0.87}CoSb$ sample has notable micron-scale porosity, despite having a gravimetric density of 95%. The Nb and Ta samples by contrast appear fully dense, in keeping with the 100% gravimetric densities (Table 1). Secondly, the EBSD data show a gradual decrease of the average grain size diameter from ~3.2 μm (V) to ~0.80 μm (Nb) and ~0.43 μm (Ta). This trend is in keeping with the increasing refractory nature of the A-elements. The EDS mapping reveals that all

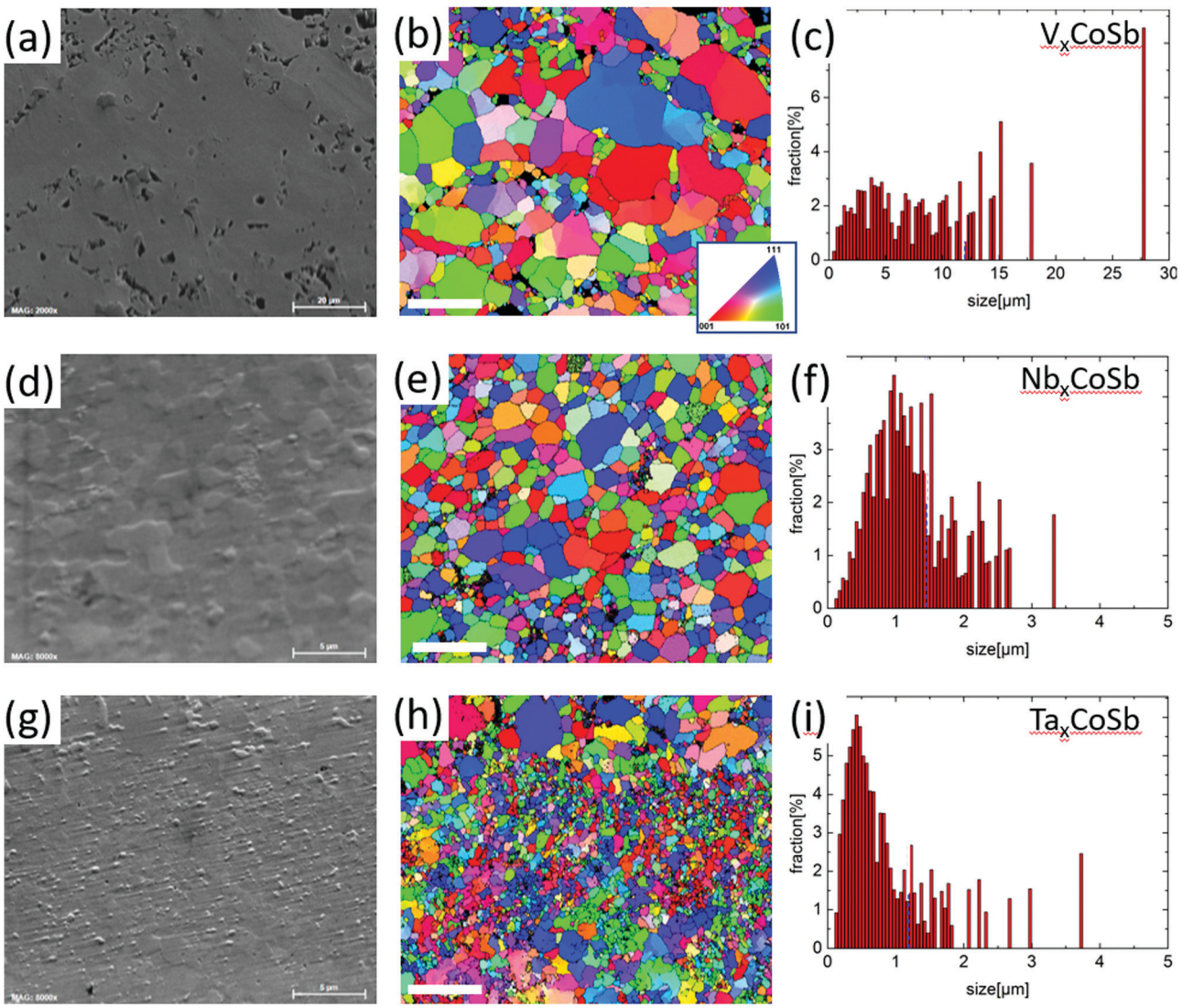

Fig. 3 (Left) Scanning electron microscopy, (middle) false-coloured electron backscatter diffraction (EBSD) images and (right) measured grain size distributions of (a–c) $V_{0.87}CoSb$, (d–f) $Nb_{0.85}CoSb$ and (g–i) $Ta_{0.81}CoSb$, illustrating the internal structure and granularity. The scale-bars in the SEM images are the same as those in the EBSD and are, respectively, 20 μm, 5 μm and 5 μm in length. Colours in the EBSD images relate to the orientation of crystallographic grains, as indicated in the key in panel (b); the random distribution of orientations enables rapid discrimination of grain sizes. A mean diameter was calculated for each grain picked out by black lines in the EBSD and used to construct the distributions in panels (c, f and i).

A_xCoSb samples are largely phase pure HHs with no obvious variation in composition. The elemental maps for $V_{0.87}$CoSb indicate fractionally more oxide formation than for the other two samples. The obtained HH compositions, averaged across all HH grains measured in the samples, are given in Table 1.

Electrical properties

All samples exhibit negative $S(T)$ values, indicating n-type conduction (Fig. 4a). There is a clear increase in $S(T)$ as the A site element becomes heavier; in addition, the Ta sample has a much steeper increase. The V and Nb samples have a similar metal-like $\rho(T)$ that increases across the temperature range whilst the Ta sample, by contrast, is much less conductive and has a gradually decreasing convex temperature dependence. This non-standard temperature dependence is not typical of either degenerate or non-degenerately doped semiconductors and is likely linked to its microstructure, consisting of many nano-scale grains. The highest power factor, S^2/ρ = 2.7 mW m^{-1} K^{-2}, is observed for the $Nb_{0.85}$CoSb composition, while $V_{0.87}$CoSb has S^2/ρ = 2.2 mW m^{-1} K^{-2} (Fig. 4c). Both compositions are characterised by a S^2/ρ plateau above ~800 K (V) and ~700 K (Nb), reflecting the saturation of S and increasing ρ. Increasing the temperature above 950 K is expected to lead to a reduction in S^2/ρ. The Ta sample with its high ρ values has a S^2/ρ that increases linearly from ~0.1 mW m^{-1} K^{-2} at 323 K to a maximum ~0.7 mW m^{-1} K^{-2} at 950 K. However, it is worth emphasising that this might not reflect its intrinsic behaviour but instead be a result of microstructure effects.

Hall measurements were undertaken to gain further insight in the electrical properties of these materials. The n_H, Hall mobilities (μ_H) and S and ρ for these samples are summarised in Table 2. Significantly, n_H has a linear dependence on the nominal free electron count (VEC-18) from the Rietveld compositions (see inset to Fig. 4b), confirming the validity of our structural analysis, and the tendency for a reduced occupation of the X-site from V to Nb to Ta.[20] To gain insight into possible changes in the electronic structure of these materials, Single Parabolic Band analysis was undertaken, following approaches outlined in the literature (*e.g.* ref. 26). This led to a significant result, namely the gradual decrease of the electronic density of states band masses from m^* = 12.8m_e (V), to m^* = 9.6m_e (Nb) and m^* = 5.9m_e (Ta), demonstrating that the A-metal impacts on the electronic bandstructure. The value for the Nb sample is in good agreement with m^* = 8–10m_e from the literature.[11,27] The decrease of $m^* = N_v^{2/3} m_b$ signals either a decrease in valley degeneracy (N_v) or increasingly dispersive electronic bands (reduced m_b) for the pockets that contribute the electrical transport. The more diffuse 4d and 5d orbitals for the heavier A elements are known to afford better orbital overlap and increased bandwidths, which is in keeping with the observed trend. The carrier mobility for the Nb sample is largest at μ_H = 4.2 cm^2 V^{-1} s^{-1}, which is comparable to the highest literature values.[11,27] The mobility is lower for the V sample with μ_H = 1.2 cm^2 V^{-1} s^{-1}, which is partially due to its higher m^* and n_H but is also likely to be linked to the observed porosity. The magnitude is in keeping with reported data for nominally stoichiometric VCoSb.[27] The A = Ta sample has μ_H = 0.3 cm^2 V^{-1} s^{-1}, despite its lower m^* and n_H, which reflects its microstructure consisting of many very small grains.

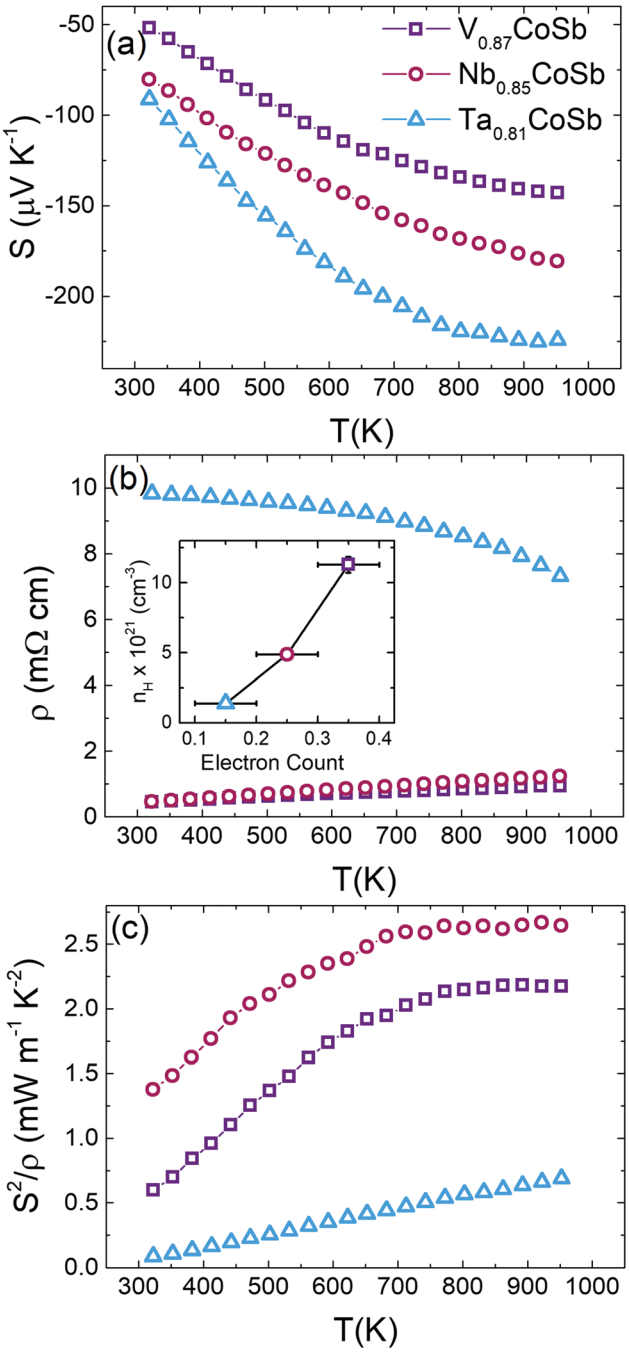

Fig. 4 Temperature dependence of (a) the Seebeck coefficient (S), (b) the electrical resistivity (ρ), and (c) the power factor (S^2/ρ) for $V_{0.87}$CoSb, $Nb_{0.85}$CoSb and $Ta_{0.81}$CoSb. The inset to panel (b) shows the linear dependence of the Hall carrier concentration (n_H) on formal electron count (VEC – 18).

Thermal conductivity

Fig. 5a shows the total thermal conductivity (κ) for all samples. The measured thermal diffusivities (α) and heat capacities (C_p)

Table 2 Nominal electron count, Seebeck coefficient (S), electrical resistivity (ρ), Hall carrier concentration (n_H), Hall mobility (μ_H) and density of states effective mass (m^*) for the A_xCoSb samples. Data collected at room temperature

Composition	Electron count	S ($\mu V\ K^{-1}$)	ρ (mΩ cm)	n_H ($\times 10^{21}$ cm^{-3})	μ_H (cm^2 V^{-1} s^{-1})	$m^*(m_e)$
$V_{0.87}CoSb$	0.35(5)	−53	0.44	11.3	1.2	12.8
$Nb_{0.85}CoSb$	0.25(5)	−68	0.31	4.9	4.2	9.6
$Ta_{0.81}CoSb$	0.15(5)	−93	15.3	1.4	0.3	5.9

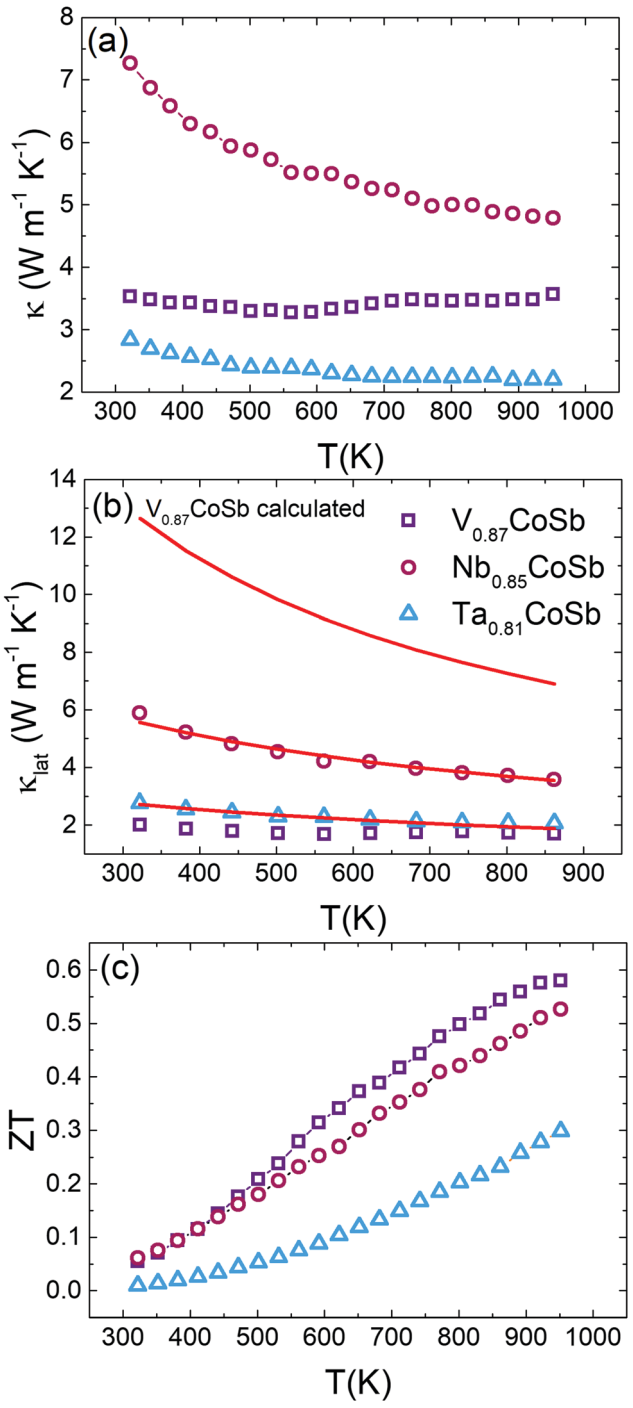

Fig. 5 Temperature dependence of (a) the total thermal conductivity (κ), (b) the lattice thermal conductivity (κ_{lat}) and (c) the dimensionless figure of merit (ZT) for $V_{0.87}CoSb$, $Nb_{0.85}CoSb$ and $Ta_{0.81}CoSb$. The solid red lines in panel (b) are calculated using the Callaway model, see manuscript text.

are shown in Fig. S5 (ESI†). $Nb_{0.85}CoSb$ has the highest κ and the value for $Ta_{0.81}CoSb$ is much reduced by comparison. $V_{0.87}CoSb$ has an unusual, nearly temperature independent, $\kappa(T)$ between 323–950 K, which is not in line with the observed decreasing $\kappa(T)$ trends for the Nb and Ta samples. Subtraction of κ_{el} using the Wiedemann–Franz law yields the lattice thermal conductivities (κ_{lat}) that are plotted in Fig. 5b. The temperature dependence of the Lorenz number (L) and κ_{el} are shown in Fig. S6 (ESI†). The $\kappa_{lat}(T)$ values confirm the gradual decreasing temperature dependence for the Nb and Ta samples. $\kappa_{el} \sim 1.5$ W m^{-1} K^{-1} for the V sample, leading to κ_{lat} values of 2.0 W m^{-1} K^{-1} at 323 K and 1.8 W m^{-1} K^{-1} at 950 K. These values are lower than those for $Ta_{0.81}CoSb$, and around three times lower than the Nb sample. The ultralow κ_{lat} for the V sample goes against the usual dependence on average atomic mass, where lower sound velocities (v_s) for heavier elements tend to favour lower κ_{lat}.

To gain a better understanding of the thermal transport in these three samples, $\kappa_{lat}(T)$ was modelled using the Callaway model. As a first step the Debye temperatures (θ_D) and v_s were estimated from the average room temperature ADPs listed in Table S1 (ESI†) using the procedure from ref. 28 as followed in our earlier work.[10] The resulting θ_D and v_s for the A_xCoSb samples are listed in Table 3 and follow the expected trends based on increasing average atomic mass. θ_D values decrease from V (279(6) K) to Nb (221(3) K) and Ta (192(2) K), signalling a softening of the lattice for the heavier A atoms. This is reflected in v_s, which gradually reduces. For comparison, θ_D = 361(3) K for NbCoSn,[10] demonstrating that the X-site vacancies lead to a softening of the lattice, as expected when removing a fraction of the chemical bonds in the structure. The low κ_{lat} of the V sample is therefore not explained by an anomalous θ_D or v_s value, which both fit in with the behaviour of the Nb and Ta samples.

The Callaway model is based on the Debye approximation for C_p for a monoatomic cubic lattice and allows for phonon scattering from boundaries between grains, point-defects and other phonons through the Umklapp mechanism. This leads to the following expressions:[29–31]

$$\kappa_{lat} = \frac{k_B}{2\pi^2 v_s}\left(\frac{k_B T}{\hbar}\right)^3 \int_0^{\frac{\theta_D}{T}} \frac{x^4 e^x}{\tau_{ph}^{-1}(e^x-1)^2} dx \quad (1)$$

where $x = \hbar\omega/k_B T$ is the reduced phonon energy, k_B is Boltzmann's constant, $\hbar$ is the reduced Planck's constant, and τ_{ph} is the total phonon relaxation rate defined as

$$\tau_{ph}^{-1} = \frac{v_s}{D} + A_{PD}\omega^4 + B_U T\omega^2, \quad (2)$$

Table 3 Lattice thermal conductivity (κ_{lat}) at 322 K, Debye temperature (θ_D), velocity of sound (v_s), calculated mass fluctuation disorder parameter (Γ_M), theoretical and fitted Umklapp scattering factors (B_U) for the A_xCoSb compositions

Composition	$\kappa_{lat,322K}$ (W m^{-1} K^{-1})	θ_D (K)	v_s (m s^{-1})	Γ_M	L (μm)	$B_{U,calc}$[a] (10^{-18} s K^{-1})	$B_{U,fit}$ (s K^{-1})
$V_{0.87}CoSb$	2.0	270(6)	2339(50)	0.016	3.2	1.10	—
$Nb_{0.85}CoSb$	5.9	221(3)	1951(25)	0.044	0.80	1.65	1.45
$Ta_{0.81}CoSb$	3.0	192(2)	1696(20)	0.099	0.43	2.07	2.06

[a] The Gruneisen parameter was set to 1.0 for all three compositions.

where D is the average grain size, A_{PD} and B_U are the strengths of point-defect and Umklapp scattering, respectively. A_{PD} can be estimated using

$$A_{PD} = \frac{V}{4\pi v_s^3}\Gamma. \quad (3)$$

Here, V is the volume per atom and Γ is the disorder scattering parameter, which was calculated from the mass fluctuations caused by introduction of vacancies using:[32]

$$\Gamma = \frac{1}{3}q(1-q)\left(\frac{m_A}{m_{av}}\right)^2. \quad (4)$$

Here, q is the fraction of X-site vacancies and m_A is the mass of the A atoms occupying the X-site. We note that the site inversion of V and Co could contribute to point-defect scattering but the similarity in mass and size of V and Co atoms suggest this contribution to be small. Strain fluctuations due to size differences were also excluded as this leads to unphysically large values for vacancy compositions.[32] Finally, B_U was calculated from:

$$B_U = \left(\frac{V}{6\pi^2}\right)^{1/3}\frac{2k_B\gamma^2}{m_{av}v_s^3}. \quad (5)$$

Here, γ is the Grüneisen parameter and m_{av} is average mass.

The magnitude of A_{PD} was calculated using eqn (3) and (4) and kept fixed through the fitting. D was estimated from the average grain size from the EBSD data and was also kept fixed. Values for the disorder parameter Γ and grain size D are given in Table 3. Starting values of B_U were calculated and are compared against the fitted values in Table 3. We find that $\kappa_{lat}(T)$ for the Nb and Ta samples is well described using the Callaway model (see Fig. 5b, full lines), where $\gamma = 1$ gives good agreement between predicted and experimental B_U values (Table 3). The $\gamma = 1$ value is in keeping with the largely harmonic bonding in HHs. The limited temperature dependence of $\kappa_{lat}(T)$ for the Ta sample is linked to the small grains (B = 0.44 μm), leading to substantial boundary scattering. Fits with $B > 1$ μm could not satisfactorily reproduce the data. In case of the Nb sample, a comparable fit can be obtained with B_U at the calculated value and B = 1.8 μm, suggesting that boundary scattering is less important for this composition. The good agreement between experimental and calculated $\kappa_{lat}(T)$ for the Nb and Ta samples, from an essentially parameter-less fit, suggests that the behaviour for "ideal" $V_{0.87}CoSb$ can be predicted using the Callaway model. The calculated $\kappa_{lat}(T)$ for $V_{0.87}CoSb$ using the input parameters as listed in Table 3 (D = 3.2 μm; Γ = 0.016; $B_U = 1.12 \times 10^{-18}$ s K^{-1}) is shown in Fig. 5b and yields κ_{lat} values that are much greater and with a stronger temperature dependence than the experimental trends. The discrepancy between the predicted and observed values will be discussed below.

Figure of merit

The highest ZT is observed for $V_{0.87}CoSb$ with a maximum of 0.58 at 950 K (Fig. 5c). This value is slightly higher than $ZT \sim 0.5$ at 973 K for "stoichiometric" VCoSb, which has a comparable S^2/ρ = 2.5 mW m^{-1} K^{-2} but slightly larger κ = 4.4 W m^{-1} K^{-1} at 973 K.[8] $Nb_{0.85}CoSb$ has a maximum ZT = 0.52 at 950 K, which is consistent with previous values from nominally stoichiometric NbCoSb (ref. 7 and 10) and Sn substituted samples ($ZT \sim 0.5$ at 950 K for $NbCoSb_{0.8}Sn_{0.2}$);[27] but is ~33% lower than the best Nb_xCoSb composition with adjusted stoichiometry (ZT = 0.75 at 950 K for x = 0.82).[11] This discrepancy is mostly caused by a lower κ_{lat} = 2.25 W m^{-1} K^{-1} at 950 K for those samples that were processed *via* levitation melting. $Ta_{0.81}CoSb$ reaches ZT = 0.3 at 950 K, which is limited by the high ρ values.

Discussion

Structural analysis and Hall measurements both confirm the reported tendency for a reduced occupancy of the X-site from V to Nb to Ta, and thereby lower n-type carrier concentrations. We find values of x = 0.87 (V), x = 0.85 (Nb) and x = 0.81 (Ta), which were observed for both the trial series and when specifically targeted, suggesting that these are "preferred" values under the used synthesis conditions. The reduced X-site occupancy has been linked to the cost of filling antibonding conduction band states.[20] Our Hall data support this with the reduced m^* from V to Nb to Ta signalling an increase in band dispersion. This results in a higher cost for band filling, leading to reduced X-site occupancies. Whilst our data show that each system has a preferred vacancy concentration, this does not mean that it cannot be controlled, as has indeed been done for the Nb_xCoSb HHs by varying the nominal composition between $0.8 \leq x \leq 1$.[11] The reported n_H suggests that the actual variation is between $0.81 \leq x \leq 0.87$, assuming each Nb beyond x = 0.8 donates 5 electrons. This is in good agreement with the stability window ($\Delta x \sim 0.05$ at 1073 K) reported by Anand *et al.*[20] It is likely that the V and Ta systems have a similar stability window over which the vacancy concentration can be varied and this should be pursued to optimise ZT. Using n_H to estimate the X-site occupancy, leads to x = 0.91 (V), x = 0.85 (Nb) and x = 0.81 (Ta), where the slight overestimate for the V sample may be linked to V/Co inversion.

The second important result pertains to the microstructure, where both porosity and grain-size variations were discovered

between samples. A gradually decreasing average grain size was observed from V to Nb to Ta, a reduction that scales with the increased melting point of the A elements and suggests that much higher sintering and consolidation temperatures are needed for the Ta sample. On the other hand, despite its largest average grain size diameter ($\sim$3.2 μm) and 95% gravimetric density, the V sample has many micron-sized pores that reduce the connectivity of grains.

The other significant result is the unexpectedly low κ_{lat} for the V sample. Our results demonstrate a gradual decrease in θ_D and a softening of the lattice from V to Nb to Ta, consistent with the increased mass of the A atom and the increasing amount of chemical bonds removed from the structure. The observation of the lowest κ_{lat} for the V sample is therefore highly surprising. The κ_{lat} for the Nb and Ta samples is explained well within the Callaway framework, but this model substantially over-estimates κ_{lat} for $V_{0.87}$CoSb. The two main differences compared to the other samples are the presence of V/Co inversion and the micron-scale porosity and it is tempting to speculate that one of these differences accounts for the failure of the model. The impact of V/Co disordering in terms of mass fluctuations and lattice strain is small and is not expected to explain the low κ_{lat} values. Literature on nominally stoichiometric VCoSb with similar $\sim$95% gravimetric densities, prepared using arc-melting, ball-milling and hot-pressing, reveals a comparable κ_{lat} = 3 W m^{-1} K^{-1}.[8] We therefore surmise that the observed ultralow κ is generic and linked to the microstructure of these samples. The microstructure also affects the electrical properties with a reduced μ_H compared to the Nb sample. However, the observed S^2/ρ remain competitive and the electrical transport is therefore less affected than κ_{lat}. The surface area porosity based on analysis of Fig. 3a is $\sim$14%, which is much larger than the $\sim$5% estimated from density measurements. This pushes this material in the domain where classical porosity corrections no longer hold.[33,34] To fully analyse the low κ_{lat}, multilength scale modelling considering the nature of the porosity and the phonon spectrum needs to be undertaken.

Finally, the ultralow κ for the $V_{0.87}$CoSb sample is coupled to a large n_H and modest μ_H = 1.2 cm^2 V^{-1} s^{-1}, enabling S^2/ρ = 2.3 mW m^{-1} K^{-2} and ZT = 0.6. It may be possible to improve μ_H through sample processing, while the vacancy concentration could be changed to control n_H and optimise ZT. The Nb sample has μ_H = 4.2 cm^2 V^{-1} s^{-1} and S^2/ρ = 2.7 mW m^{-1} K^{-2}, which are amongst the largest values in the literature,[11,27] demonstrating the viability of the powder-based synthesis route for the Nb samples. The performance of the Ta sample is limited by its low μ_H and large ρ, which is caused by the nanoscale grain sizes that also affect κ_{lat}. For the Ta system, the focus should be on increasing the average grain size, *e.g.* by higher temperature processing, which will afford increases in S^2/ρ, whereas even for B = 5 μm, κ_{lat} increases by only $\sim$0.8 W m^{-1} K^{-1} at 323 K from the Callaway analysis. In case of the V system, work should focus on controlling the micron-scale porosity evident in Fig. 3a to explore to what extent it is possible to increase μ_H and reduce κ_{lat}.

Conclusions

To conclude, the topical A_xCoSb (X = V, Nb, Ta) HHs form with different "preferred" vacancy concentrations, increasing from 13% (V) to 15% (Nb) and 19% (Ta). This is explained by the increased cost of populating antibonding conduction band states, which limits the maximum achievable n-type carrier concentration. The anomalously low κ_{lat} for $V_{0.87}$CoSb was modelled using the Callaway approximation but cannot be understood within this framework, whilst the Nb and Ta compositions can. Further work is needed to understand the low κ_{lat}, which may be linked to porosity, and could offer a route to improved *ZT via* microstructure control. Competitive maximum figures of merit of ZT = 0.5–0.6 were observed for A = V, Nb at 950 K, whilst A = Ta has ZT = 0.3 at the same temperature, largely due to a higher electrical resistivity linked to smaller grain sizes compared to the other compositions.

Conflicts of interest

There are no conflicts of interest to declare.

Acknowledgements

The EPSRC is acknowledged for funding the research on half-Heusler thermoelectrics and instrumentation (EP/N01717X/1, EP/N017218/1 and EP/P001483/1) and for a studentship for DAF. The STFC is acknowledged for allocation of neutron scattering beamtime at the ISIS facility (RB1810470 and Xpress 1890125). Raw data upon with this publication is based can be accessed at http://dx.doi.org/10.5525/gla.researchdata.753.

References

1 *CRC Handbook of Thermoelectrics*, ed. D. M. Rowe, CRC Press, Boca Raton, 1995.
2 *Thermoelectrics and its Energy Harvesting* ed. D. M. Rowe, CRC Press, Boca Raton, 2012.
3 L. H. Huang, Q. Y. Zhang, B. Yuan, X. Lai, X. Yan and Z. F. Ren, *Mater. Res. Bull.*, 2016, **76**, 107–112.
4 J. W. G. Bos and R. A. Downie, *J. Phys.: Condens. Matter*, 2014, **26**, 433201.
5 T. J. Zhu, C. G. Fu, H. H. Xie, Y. T. Liu and X. B. Zhao, *Adv. Energy Mater.*, 2015, **5**, 1500588.
6 T. Graf, C. Felser and S. S. P. Parkin, *Prog. Solid State Chem.*, 2011, **39**, 1–50.
7 L. Huang, R. He, S. Chen, H. Zhang, K. Dahal, H. Zhou, H. Wang, Q. Zhang and Z. Ren, *Mater. Res. Bull.*, 2015, **70**, 773–778.
8 H. Zhang, Y. Wang, L. Huang, S. Chen, H. Dahal, D. Wang and Z. Ren, *J. Alloys Compd.*, 2016, **654**, 321–326.
9 W. G. Zeier, S. Anand, L. Huang, R. He, H. Zhang, Z. Ren, C. Wolverton and G. J. Snyder, *Chem. Mater.*, 2017, **29**, 1210–1217.
10 D. A. Ferluccio, R. I. Smith, J. Buckman and J. W. G. Bos, *Phys. Chem. Chem. Phys.*, 2018, **20**, 3979–3987.
11 K. Xia, Y. Liu, S. Anand, J. G. Snyder, J. Xin, J. Yu, X. Zhao and T. Zhu, *Adv. Funct. Mater.*, 2018, **28**, 1705845.

12 M. Gurth, G. Rogl, V. Romaka, A. Grytsiv, E. Bauer and P. Rogl, *Acta Mater.*, 2016, **104**, 210–222.
13 J. J. Yu, C. G. Fu, Y. T. Liu, K. Y. Xia, U. Aydemir, T. C. Chasapis, G. J. Snyder, X. B. Zhao and T. J. Zhu, *Adv. Energy Mater.*, 2018, **8**, 1701313.
14 L. Chen, S. Gao, X. Zeng, A. M. Dehkordi, T. M. Tritt and S. J. Poon, *Appl. Phys. Lett.*, 2015, **107**, 041902.
15 S. A. Barczak, J. E. Halpin, J. Buckman, R. Decourt, M. Pollet, R. I. Smith, D. A. MacLaren and J. W. G. Bos, *ACS Appl. Mater. Interfaces*, 2018, **10**, 4786–4793.
16 W. J. Xie, Y. G. Yan, S. Zhu, M. Zhou, S. Populoh, K. Galazka, S. J. Poon, A. Weidenkaff, J. He, X. F. Tang and T. M. Tritt, *Acta Mater.*, 2013, **61**, 2087–2094.
17 J. Makongo, D. Misra, X. Zhou, A. Pant, M. Shabetai, X. Su, C. Uher, K. Stokes and P. Poudeu, *J. Am. Chem. Soc.*, 2011, **133**, 18843–18852.
18 R. A. Downie, R. I. Smith, D. A. MacLaren and J. W. G. Bos, *Chem. Mater.*, 2015, **27**, 2449–2459.
19 X. A. Yan, G. Joshi, W. S. Liu, Y. C. Lan, H. Wang, S. Lee, J. W. Simonson, S. J. Poon, T. M. Tritt, G. Chen and Z. F. Ren, *Nano Lett.*, 2011, **11**, 556–560.
20 S. Anand, K. Xia, T. Zhu, C. Wolverton and J. G. Snyder, *Adv. Energy Mater.*, 2018, 1801409.
21 B. H. Toby, *J. Appl. Crystallogr.*, 2001, **34**, 210–213.
22 A. C. Larson and R. B. Von Dreele, *Los Alamos National Laboratory Report LAUR*, 2000, pp. 86–748.
23 B. Beausir and J.-J. Fundenberger, *ATOM - Analysis Tools for Orientation Maps*, Université de Lorraine – Metz, 2015, http://atom-software.eu, software package.
24 R. He, L. H. Huang, Y. M. Wang, G. Samsonidze, B. Kozinsky, Q. Y. Zhang and Z. F. Ren, *APL Mater.*, 2016, **4**, 104804.
25 S. Anand, K. Xia, V. I. Hegde, U. Aydemir, V. Kocevski, T. Zhu, C. Wolverton and J. G. Snyder, *Energy Environ. Sci.*, 2018, **11**, 1480–1488.
26 H. H. Xie, H. Wang, Y. Z. Pei, C. G. Fu, X. H. Liu, G. J. Snyder, X. B. Zhao and T. J. Zhu, *Adv. Funct. Mater.*, 2013, **23**, 5123–5130.
27 L. Huang, Q. Zhang, Y. Wang, R. He, J. Shuai, J. Zhang, C. Wang and Z. Ren, *Phys. Chem. Chem. Phys.*, 2017, **19**, 25683–25690.
28 B. C. Sales, B. C. Chakoumakos, D. Mandrus and J. W. Sharp, *J. Solid State Chem.*, 1999, **146**, 528–532.
29 J. Callaway, *Phys. Rev.*, 1959, **113**, 1046–1051.
30 A. Petersen, S. Bhattacharya, T. M. Tritt and S. J. Poon, *J. Appl. Phys.*, 2015, **117**, 035706.
31 E. S. Toberer, A. Zevalkink and G. J. Snyder, *J. Mater. Chem.*, 2011, **21**, 15843–15852.
32 J. Yang, G. Meisner and L. Chen, *Appl. Phys. Lett.*, 2004, **85**, 1140–1142.
33 R. H. Tarkhanyan and D. G. Niarchos, *Int. J. Therm. Sci.*, 2013, **67**, 107–112.
34 R. H. Tarkhanyan and D. G. Niarchos, *APL Mater.*, 2014, **2**, 076107.